

Near detector simulation studies for CP violation discovery with ESSnuSB

Bachelor's Thesis

Author: In-Pyo Yeo

15 hp, 6 months

Supervisors: Joochun Park and Joakim Cederkäll
Lund University

VT 2019



LUND
UNIVERSITY

Department of Physics
Division of Nuclear Physics

Contents

1	Introduction	4
1.1	Fundamental questions in physics and cosmology	4
1.1.1	The Matter-Antimatter asymmetry	4
1.2	The role of neutrinos and neutrinos oscillations	5
1.2.1	Dirac or Majorana neutrino	5
1.2.2	Neutrino mixing parametrization	6
1.2.3	The neutrino mixing angle θ_{13}	7
2	The ESSnuSB project and its near detector	8
2.1	Future experiments for CP violation measurements	8
2.2	The ESS facility	8
2.3	Overview of the ESSnuSB	9
2.3.1	The neutrino beam	9
2.3.2	Water Cherenkov detectors	11
2.4	Typical design of a water Cherenkov detector	11
2.4.1	Migration matrices	12
3	Method	13
3.1	Water Cherenkov detector simulation software WCSim	13
3.2	Cherenkov ring reconstruction software fitQun	14
3.3	Validation of WCSim and fitQun using the HyperK geometry	14
3.4	Adaptation to the ESSnuSB near detector geometry	15
4	Results and Discussion	16
4.1	Lepton identification performance	16
4.2	Geometrical effects on the reconstruction performance	19
4.3	Preliminary migration matrices	21
5	Conclusion	21

Abstract

The neutrino oscillation experiment ESSnuSB aims to measure the CP violation phase in the lepton sector with an intense neutrino beam produced at ESS. If the CP violation is discovered, then the matter-antimatter asymmetry of the Universe can be possibly explained. In order to do this, a design study of a water Cherenkov near detector was carried out, and its geometrical parameters such as the tank size and the PMT size were evaluated using a dedicated simulation software and a previously developed reconstruction algorithm. The reconstruction results show that the electrons are less likely to be misidentified than the muons, and the misidentification percentages for electrons were highly dependent on the tank size rather than the PMT size. On the other hand, the misidentification percentages for muons were independent of both the tank size and the PMT size. Instead, other geometrical effects played a more dominant role in particle misidentification. In order to lower the misidentification percentages, more sophisticated selection cuts are suggested. Finally, 2D mappings of the input lepton energies versus the reconstructed lepton energies, known as migration matrices, were constructed for both muons and electrons. Dedicated tunes of the modified detector geometries may address a discrepancy between the input lepton energy and the reconstructed energy, while improving the particle identification accuracy. These results provided guidance on more comprehensive design studies of the near detector.

1 Introduction

1.1 Fundamental questions in physics and cosmology

Physicists recognized in the 1970s that the weak force and the electromagnetic force can be unified, and by that laid one of the foundations of the Standard Model. This unification of electricity, magnetism and some types of radioactivity showed that these forces can all be described as a single elementary force, which is now known as the electroweak force. The electroweak force is mediated by a massless force-carrying particle called the photon, and by W and Z bosons, which are about 100 times heavier than the proton. In order to explain the large masses of the W and the Z bosons, the Higgs mechanism was introduced [1]. The ATLAS and CMS experiments at CERN's Large Hadron Collider reported the discovery of a new particle in the mass region of 125 GeV in 2012. This particle is compatible with the hypothesized Higgs boson, although more research is needed to determine its exact nature.

Another recent discovery concerning the electroweak force is neutrino oscillations [2]. It has been found earlier that there are three types of neutrinos: the electron neutrino (ν_e), the muon neutrino (ν_μ) and the tau neutrino (ν_τ). The oscillations show that neutrinos can change flavours between each other. This is an important discovery, since the neutrino was earlier treated as a massless particle according to the Standard Model, while oscillations now prove that neutrinos do have mass.

1.1.1 The Matter-Antimatter asymmetry

The excess of matter compared to antimatter in the observed universe is one of the most fundamental questions in modern physics. This matter-antimatter asymmetry is expressed by the baryon-to-photon ratio [3], as,

$$\eta_B = \frac{n_b - n_{\bar{b}}}{n_\gamma}, \quad (1)$$

where n_b is the baryon density, $n_{\bar{b}}$ is the antibaryon density, and n_γ is the photon density. Baryogenesis is the hypothetical process that the baryonic asymmetry is produced in the Big Bang, due to an imbalance in the production rates of matter and antimatter. The following Sakharov conditions should be fulfilled for baryogenesis, [4]:

- violation of baryon number,
- violation of C and CP symmetry, and
- interactions out of thermal equilibrium.

CP conservation consists of two symmetry operations: charge conjugation, represented by the operator \hat{C} , and parity transformation represented by the operator \hat{P} . Charge conjugation changes matter particles into antimatter particles in the system. On the other hand, the parity transformation converts all spatial coordinates into their opposites. According to the helicity (the projection of a particle's spin on its

direction of propagation) of a relativistic particle, massless particles are predominantly left-handed and antiparticles are right-handed [5]. The combination of the CP operation would convert a left-handed particle into a right-handed antiparticle. The breaking of CP symmetry (CP violation) could result in a particle production rate different to that for an antiparticle, and thus explain the matter-dominant Universe that is observed today.

1.2 The role of neutrinos and neutrinos oscillations

As discussed above, the neutrino is a lepton, i.e. a fermion with half integer spin, with three different flavours: the muon neutrino (ν_μ), the electron neutrino (ν_e), and the tau neutrino (ν_τ). According to the Standard Model, the neutrino has been treated as a massless particle interacting via the weak field propagators, the W^\pm and Z^0 bosons [6]. However, the discovery of neutrino oscillations between the three different flavours during propagation indicates that neutrinos are massive particles and that they can have both left- and right-handed helicity. Furthermore, three mass eigenstates of neutrinos, ν_1 , ν_2 and ν_3 , can be defined. By assuming the ordering of the neutrino masses to be such that $m_2 > m_1$, two possible hierarchies exist: $m_1 < m_2 < m_3$, called the normal hierarchy, or $m_3 < m_1 < m_2$, called the inverted hierarchy. Neutrino oscillation experiments have determined the magnitude of all three mass square differences, showing that Δm_{21}^2 is much smaller than Δm_{31}^2 and Δm_{32}^2 . It has also been observed that Δm_{31}^2 and Δm_{32}^2 are close to each other [7].

The new Hyper-Kamiokande detector (HyperK) is planned to measure the neutrino mass hierarchy. The oscillation of both ν_μ into ν_e and $\bar{\nu}_\mu$ into $\bar{\nu}_e$ will be measured with the help of neutrinos produced at the opposite side of the Earth. One expected result is that there should be an enhanced probability for $\nu_\mu \rightarrow \nu_e$ if the mass hierarchy is normal, and $\bar{\nu}_\mu \rightarrow \bar{\nu}_e$ if the hierarchy is inverted [8].

1.2.1 Dirac or Majorana neutrino

Once the mass hierarchy is defined, it is possible to determine whether the neutrino particle has its own characteristic antiparticle, i.e. it is a Dirac particle, or the antiparticle is indistinguishable from the particle, i.e. it is a Majorana particle. Neutrinos with mass eigenstates ν_j can be Dirac fermions if the total lepton number carried by neutrinos is conserved by the interaction.

One method to address the two hypotheses is neutrinoless double beta decay, where an unstable atomic nucleus may emit zero neutrinos during its β decay if they are Majorana particles. This decay process is described by [7],

$$(A, Z) \rightarrow (A, Z + 2) + 2e^-, \quad (2)$$

where the lepton number is not conserved as $|\Delta L| = 2$ in this case.

1.2.2 Neutrino mixing parametrization

One of the first indications of neutrino oscillations came with the attempt to measure the neutrino flux from the Sun. Solar neutrinos are produced by fusion reactions in the proton-proton chain operating inside the Sun and in the Carbon-Nitrogen-Oxygen (CNO) cycle, where stars convert hydrogen into helium [7]. These reactions can be summarized as,

$$4p \rightarrow {}^4\text{He} + 2e^+ + 2\nu_e. \quad (3)$$

The positrons annihilate with electrons and the thermal solar energy generated can be described by the following expression,

$$4p + 2e^- \rightarrow {}^4\text{He} + 2\nu_e + 26.73 \text{ MeV} - E_\nu, \quad (4)$$

where E_ν is the energy given to the neutrinos with an average value of ~ 0.6 MeV. According to past neutrino detection experiments to verify the above processes, the observed flux of ν_e was only about one third of the predicted value. This result introduced neutrino oscillations as a possible solution to that ν_e could have oscillated into other flavours while propagating in space.

Another way that neutrino oscillations have been observed is from atmospheric neutrinos. These come from the decay products of hadronic showers, which originate in collisions between cosmic rays and atomic nuclei in the upper atmosphere [9]. For instance, the relevant processes lead to pion decays:

$$\pi^+ \rightarrow \mu^+ + \nu_\mu, \quad (5)$$

with a decay branching ratio of 0.999877; the remainder corresponds to the decay of π^+ into e^+ and ν_e [10]. The resulting μ^+ then decays in the following way:

$$\mu^+ \rightarrow e^+ + \bar{\nu}_\mu + \nu_e. \quad (6)$$

By measuring the different neutrino flavour rates, which come from different directions, i.e. from above the surface or through the Earth, neutrino oscillations were confirmed.

Finally, the same flavours of neutrinos are produced in typical accelerator-based neutrino oscillation experiments. The decays of charged pions produced during spallation reactions yield ν_μ , ν_e , $\bar{\nu}_\mu$ and $\bar{\nu}_e$. This case is discussed further below.

Neutrino oscillations occur because neutrino flavour eigenstates do not form a one-to-one correspondence with the mass eigenstates. The 3×3 neutrino mixing matrix U_{PMNS} based on the works of Pontecorvo, Maki, Nakagawa and Sakata map the flavour eigenstates to mass eigenstates via 3 neutrino mixing angles and additional parameters [7].

$$U_{PMNS} = \begin{bmatrix} c_{12}c_{13} & s_{12}s_{13} & s_{13}\exp(-i\delta_{CP}) \\ -s_{12}c_{23} - c_{12}s_{23}s_{13}\exp(i\delta_{CP}) & c_{12}c_{23} - s_{12}s_{23}s_{13}\exp(i\delta_{CP}) & s_{23}c_{13} \\ s_{12}s_{13} - c_{12}s_{23}s_{13}\exp(i\delta_{CP}) & -c_{12}s_{23} - s_{12}c_{23}s_{13}\exp(i\delta_{CP}) & c_{23}c_{13} \end{bmatrix} \times \text{diag}[1, \exp(i\frac{\alpha_{21}}{2}), \exp(i\frac{\alpha_{31}}{2})], \quad (7)$$

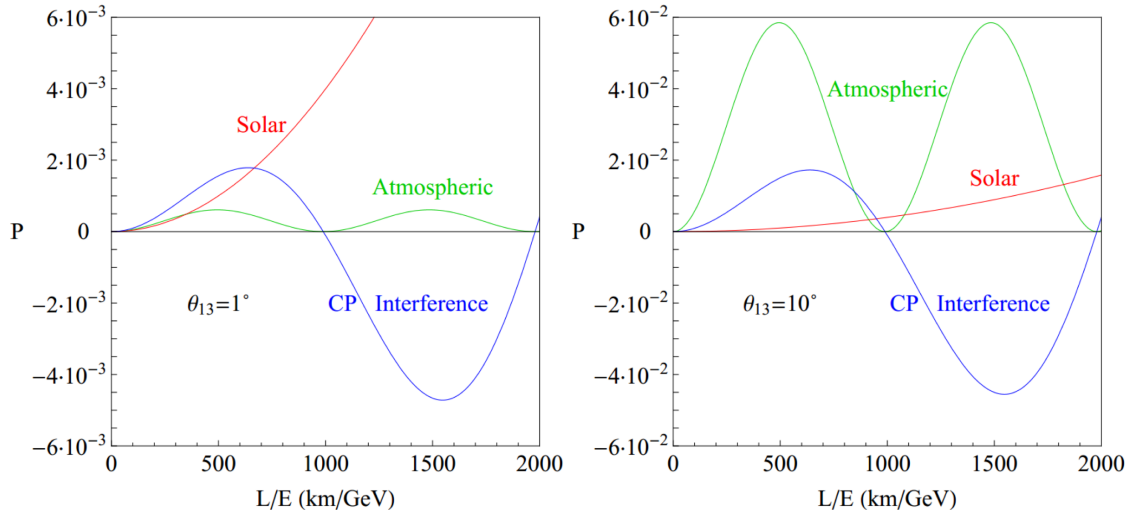


Figure 1: Neutrino oscillation probabilities in vacuum as a function of L/E for both the small and large mixing angles $\theta_{13} = 1^\circ$ (left) and $\theta_{13} = 10^\circ$ (right) [11].

where $c_{ij} = \cos \theta_{ij}$, $s_{ij} = \sin \theta_{ij}$, $\theta_{ij} = [0, \frac{\pi}{2}]$, $\delta_{CP} = [0, 2\pi]$ is the Dirac CP violation phase, α_{21} and α_{31} are the Majorana CP violation phases, and $\text{diag}[a, b, c]$ is a 3×3 matrix with diagonal elements a , b and c in their respective column/row positions.

1.2.3 The neutrino mixing angle θ_{13}

Measuring the neutrino mixing angle θ_{13} is necessary to make an experimental observation of CP violation in the leptonic sector. Previous experiments have been designed and optimized to detect CP violation at small θ_{13} . However, recent experiments such as Reno, Daya Bay and Double Chooz have shown that θ_{13} is larger than previously thought. The results gave $\sin^2 2\theta_{13} = 0.086$, and thus $\theta_{13} = 8.5^\circ$ [7].

The neutrino oscillation probability can be expressed as [11],

$$\begin{aligned}
 P_{e\mu}^\pm = P(\nu_e^{(-)} \rightarrow \nu_\mu^{(-)}) = & \\
 s_{23}^2 \sin^2 \theta_{13} \sin^2\left(\frac{\Delta_{31}L}{2}\right) + c_{23}^2 \sin^2 2\theta_{12} \sin^2\left(\frac{\Delta_{31}L}{2}\right) & \\
 + J \cos\left(\pm\delta - \frac{\Delta_{21}L}{2}\right) \sin\left(\frac{\Delta_{31}L}{2}\right) & \quad (8)
 \end{aligned}$$

where $\Delta_{ij} = \frac{\Delta m_{ij}^2}{2E_\nu}$, $J = c_{13} \sin 2\theta_{12} \sin 2\theta_{23} \sin 2\theta_{13}$ and L is the baseline distance. The first term is called ‘atmospheric’, the second is ‘solar’ and the last one is the ‘CP interference’ term.

Eq. 8 is plotted as a function of L/E (km/GeV) for two different mixing angles in Fig. 1. At the first oscillation maximum, the oscillation probability for the CP interference term, for $\theta_{13} = 1^\circ$, is greater in magnitude compared to the ‘solar’ and

‘atmospheric’ terms. However, at $\theta_{13} = 10^\circ$, the atmospheric term becomes dominant over the CP interference component at the first oscillation maximum, so that it is more advantageous to search for CP violation at the second oscillation maximum, where their magnitudes are approximately equal. This indicates that it requires a higher value of L/E for larger θ_{13} , since the experiments for CP violation discovery will encounter smaller systematic uncertainties. Therefore, a large value of θ_{13} enhances the performance for experiments that place the far detector at the second oscillation maximum compared to placing it at the first oscillation maximum.

2 The ESSnuSB project and its near detector

2.1 Future experiments for CP violation measurements

Maximum CP violation occurs when the phase $\delta_{CP} = \pm 90^\circ$. There are several proposed experiments to determine the mass hierarchy and δ_{CP} . A few of them and their characteristics are given in Table 1 [12]. It is important to notice the high intensity of neutrinos produced by ESSnuSB, since it has the highest proton exposure among the experiments. Comparing ESSnuSB with the other experiments, taking the oscillation probability in Fig. 1 into account, shows it is possible to use ESSnuSB to try to discover CP violation at the second oscillation maximum with the baseline length of 540 km. The run time ratio given in Table 1 is defined as the optimal production ratios of the neutrino and antineutrino beams for the δ_{CP} measurement.

2.2 The ESS facility

The European Spallation Source is a facility under construction in Lund, Sweden, that will provide slow neutrons to research institutions and industry. Spallation neutrons are produced using the ESS linear accelerator by bombarding a 2-GeV proton beam on a tungsten target with a beam power of 5 MW (see Fig. 2). There will be 1.1×10^{15} protons per second, contained in 14 pulses with 62.5-mA current and 2.86-ms pulse width [13].

Table 1: Comparison of future neutrino oscillation experiments. The values are taken from Ref. [12].

	T2HK	T2HKK	DUNE	ESSnuSB
Baseline (km)	295	295/1100	1300	540
Beam power (MW)	1.3	1.3	1.2	5
Total protons on target	27×10^{21}	27×10^{21}	10×10^{21}	27×10^{22}
Run time ratio ($\nu : \bar{\nu}$)	1:3	1:3	1:1	1:4



Figure 2: The schematic diagram of the ESS facility under construction in Lund, Sweden, taken from Ref. [15]

2.3 Overview of the ESSnuSB

2.3.1 The neutrino beam

The purpose of the ESSnuSB project is to use an intense neutrino beam from ESS to measure the probability for CP violation in the lepton sector. There are some requirements for modifications of the ESS linear accelerator to produce the neutrino beam and give a high CP violation discovery potential. These include acceleration of H^- ions in place of protons, reduced pulse widths, doubled pulse frequency, and higher proton-beam energy [14].

Charged pions are produced in the proton-target collisions and they are focused in the forward direction by a hadron collector (a magnetic horn). A focused neutrino beam is created since the neutrinos are produced in the pion decay and travel in the same direction as the pion that are focused by the magnetic horn. The flavour of the neutrino depends on which type of charged pion is focused while current is flowing into the magnetic horn.

The left panel in Fig. 3 shows the neutrino flavour spectrum for positive horn polarity and the right panel for negative horn polarity. In general, the most abundant neutrino flavour is the muon neutrino, which means that the magnetic horn focuses positive pions to produce ν_μ and negative pions to produce $\bar{\nu}_\mu$. The far detector should be located deep underground, 1000 m, in order to prevent cosmic ray background reaching the detector. This is necessary to be able to measure the long baseline neutrinos, proton decay, atmospheric neutrinos and supernova neutrinos in the same detector. The map in Fig. 4 shows the distance and depth of mines deeper than 1000 m from the location of the ESS site in Lund. The two potential sites for the far detector(s) of ESSnuSB are located in Garpenberg and Zinkgruvan.

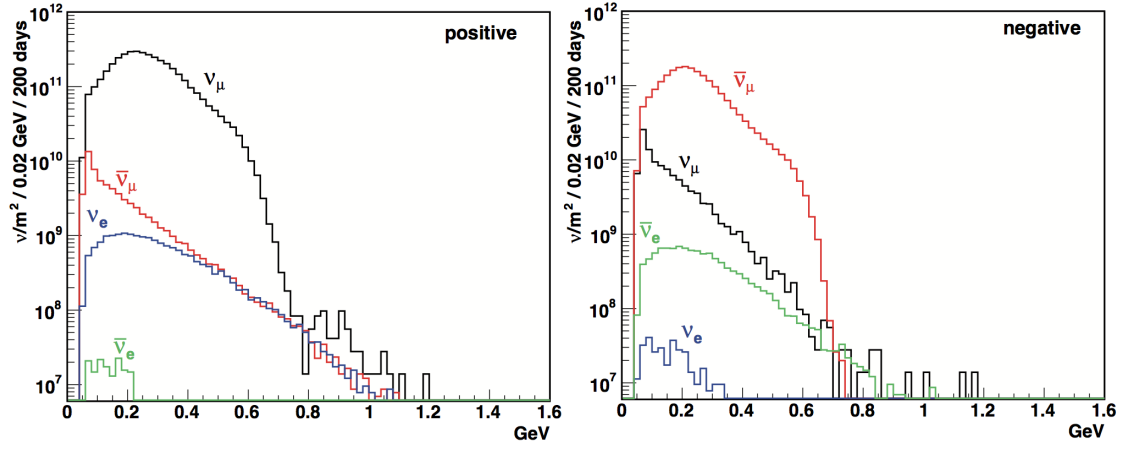


Figure 3: Expected neutrino fluence generated by a 2-GeV proton beam at the ESS, at a distance of 100 km from the target station for two opposite horn current polarities, adapted from Ref. [15].



Figure 4: The location of the ESS and prospective sites for the far detector, adapted from Ref. [15]. Garpenberg and Zinkgruvan are the most prospective sites for the far detector.

2.3.2 Water Cherenkov detectors

After the neutrino beam is produced, the near detector is used to measure the flux of neutrinos along with the interaction cross section. An important reason why a near detector should be deployed is to reduce systematic uncertainties in the neutrino flux detected at the far detector. Since the neutrino is an electrically neutral particle, it does not produce Cherenkov radiation on its own. However, the neutrino may undergo CC (charged current) interactions through the W boson and produce a charged lepton with its corresponding flavour (see Fig. 5).

A charged particle emits electromagnetic radiation called Cherenkov radiation when it propagates through a dielectric medium faster than speed of light in that medium. Cherenkov radiation is emitted around the particle's propagation path in a forward-directed cone. Assuming that the angle between the particle's direction of propagation and the cone is θ_{emit} , and the number of emitted photons is N_γ , then the following relation can be derived [16],

$$\cos \theta_{emit} = \frac{1}{n\beta} \quad (9)$$

$$N_\gamma(\lambda)d\lambda = 2\pi\alpha \times \left(1 - \frac{1}{n^2\beta^2}\right) \times \frac{d\lambda}{\lambda^2} = 2\pi\alpha \times \sin^2 \theta_{emit} \times \frac{d\lambda}{\lambda^2} \quad (10)$$

where β is the speed of the particle divided by the speed of light (v/c), n is the refractive index of the medium, λ is the wavelength of the emitted light, and α is the fine structure constant.

The neutrino can also undergo NC (neutral current) interactions through the Z boson in the medium. Neutral pions (π^0) can be produced from the NC interaction, which contribute to background events [17].

A produced charged lepton from the CC interaction gives rise to a Cherenkov cone which can be detected in the shape of a circular ring at the detector wall covered with optical photon detectors. Electrons produce a fuzzy edge of the Cherenkov ring, while a clearer edge is produced by muons. This is because the EM showers produced when an electron propagates through the medium cause emission of γ -rays and electron-positron pairs as the initial electron loses its energy [6]. Then a large fraction of the Cherenkov light is distributed in different directions.

A decay of π^0 into two γ rays leads to two electromagnetic showers and their Cherenkov rings. The π^0 production is one of the most significant sources of background, since the escape of one of the two γ rays can result in an event which mimics an electron signal.

2.4 Typical design of a water Cherenkov detector

The outermost part of a water Cherenkov detector is typically covered by photomultiplier tubes (PMTs), which is one possible detector for Cherenkov radiation [17]. A PMT consists of several electrodes such as one cathode, a number of dynodes in a sequence and an anode. Between the electrodes, a voltage is applied where each subsequent electrode has a higher positive potential than the previous one. The cathode

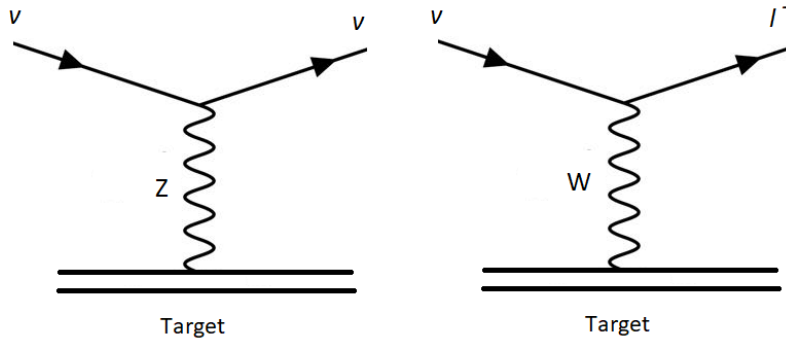


Figure 5: Feynmann diagrams for the NC (left) and CC (right) interactions of neutrinos with target matter.

is exposed to light, leading to an electron being emitted at the photo-cathode when a photoelectric effect occurs. The primary electron is then accelerated into the first dynode when the voltage is applied on the tube. Then the primary electron kicks out secondary electrons in the dynode, which are then accelerated towards the next dynode. This process is repeated until the amplified electron signal reaches the anode.

In this project, the sizes of the PMTs and the detector dimensions were adjusted in a Geant4 simulation. The details on the geometrical parameters will be discussed in section 3.4.

2.4.1 Migration matrices

The incident neutrino energy is reconstructed in the detector using the following steps: reconstruction of the interaction vertex, determination of the direction of propagation of the lepton, particle identification, rejection of the background NC interactions, and determination of the lepton momentum [19]. The initial neutrino energy is inferred from the direction and momentum of the lepton by making the assumption that its interactions are Charged Current (CC) and quasielastic (QE). The incident neutrino energy (E_ν) can be expressed by,

$$E_\nu = \frac{m_N E_l - m_l^2/2}{m_N - E_l + P_l \cos\theta_l}, \quad (11)$$

where m_N and m_l are the nucleon and lepton masses, respectively. E_l and P_l are the outgoing lepton energy and momentum, and θ_l is the lepton direction with respect to the neutrino.

It is important to determine the relationship between the incoming neutrino energy spectrum and the reconstructed energy spectrum, since it is impossible to measure the neutrinos' energies directly. The mappings of the two quantities are called migration matrices. An example of a migration matrix is shown in Fig. 6. Different migration matrices may be constructed for signal and background reaction channels, such as CC and NC. They are used to project back the expected energy distribution of neutrinos produced at the target. They may be used to assess to what extent the migration matrices for a near detector can cancel systematic errors with those for a far detector.

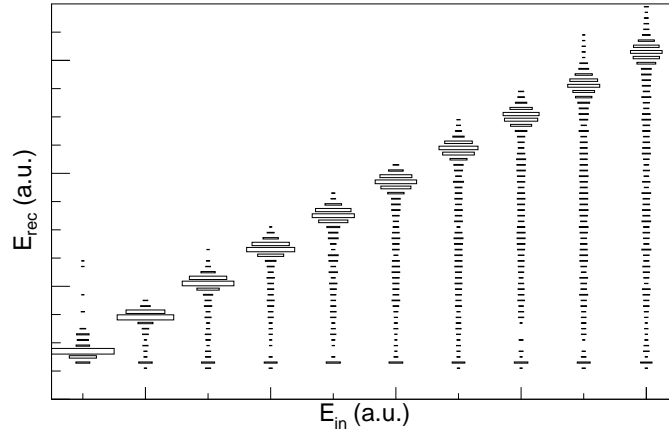


Figure 6: Migration matrix for μ^- as a function of the input energies versus reconstructed energies.

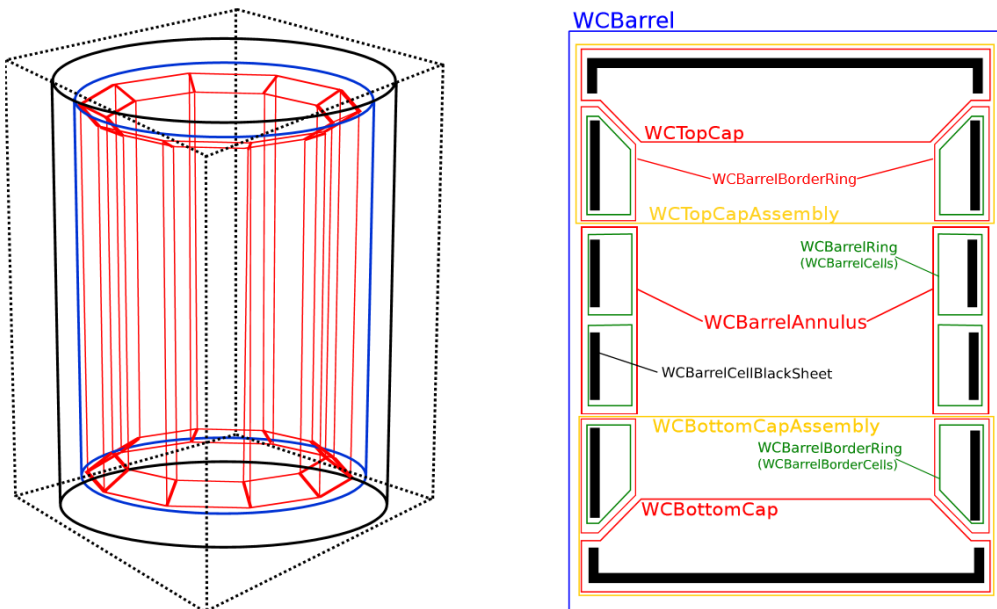


Figure 7: 3D and 2D diagrams of a simulated water Cherenkov detector via WCSim, taken from Ref. [18].

3 Method

3.1 Water Cherenkov detector simulation software WCSim

WCSim [18] is a simulation package for Cherenkov detectors based on the Geant4 framework, which is used for particle interactions with matter. The geometry of PMTs in WCSim is defined by a pre-defined set of parameters and internal algorithms concerning their placement, so that simulations involving different geometries can be easily run with only a few changes in the parameter settings (see Fig. 7). Parameters such as the size, thickness, height and PMT type can be varied.

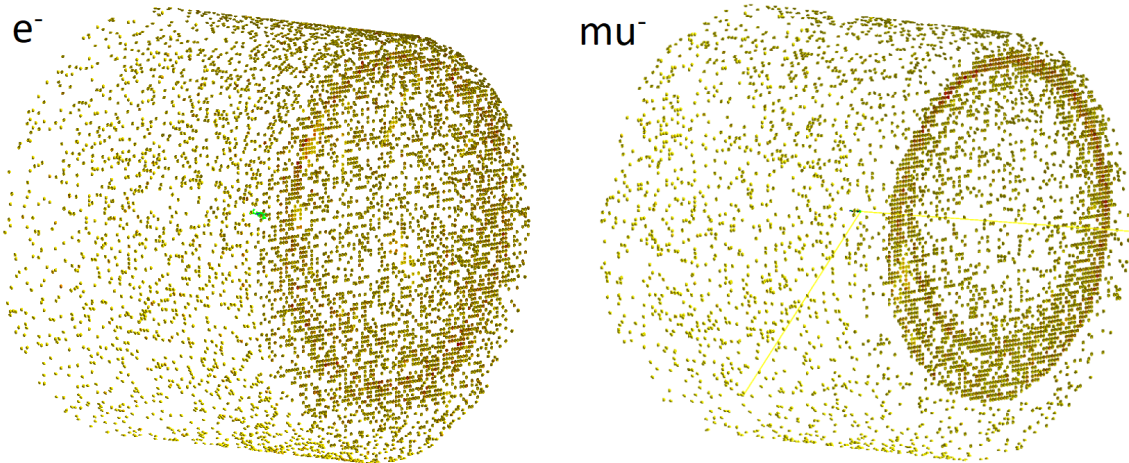


Figure 8: Event displays of Cherenkov radiation from electrons and muons at 500 MeV inside a simulated HyperK geometry with WCSim.

3.2 Cherenkov ring reconstruction software fitQun

The fitQun [20, 21] software reconstructs events in water Cherenkov detectors and produces output that can be analysed further. The reconstruction algorithm employs a maximum likelihood function of event hypotheses \mathbf{x} , which specify 8 parameters: particle type, vertex coordinates (x, y, z, t) and momentum (\vec{p}) . The likelihood function is expressed as,

$$L(\mathbf{x}) = \prod_j^{\text{unhit}} P_j(\text{unhit} | \mathbf{x}) \prod_i^{\text{hit}} P_i(\text{hit} | \mathbf{x}) f_q(q_i | \mathbf{x}) f_t(t_i | \mathbf{x}), \quad (12)$$

where the likelihood $L(\mathbf{x})$ is a product of the probabilities of the hit/unhit PMTs and the probability density functions f_q and f_t , which characterize the charge and time response functions of the PMTs hit by optical photons, respectively. Thus the reconstruction output corresponds to the hypothesis \mathbf{x} with the highest likelihood value.

3.3 Validation of WCSim and fitQun using the HyperK geometry

The first step in this work was to validate the installation of the two programs using a known geometry. Four different leptons e^+ , e^- , μ^+ , and μ^- were simulated inside of the HyperK detector volume to produce Cherenkov radiation into the curved walls of the detector (see Fig. 8). The energies of the leptons were varied from 100 MeV to 500 MeV. These settings were changed in a WCSim macro file before each simulation was started. After the simulation process was complete, the reconstruction software fitQun was run on the simulation output files.

The reconstructed energy spectra for these charged leptons, for different input energies, are shown in Fig. 9. It is clear that the electron events are better reconstructed at lower energies. However, the energy reconstruction for muons improves at higher

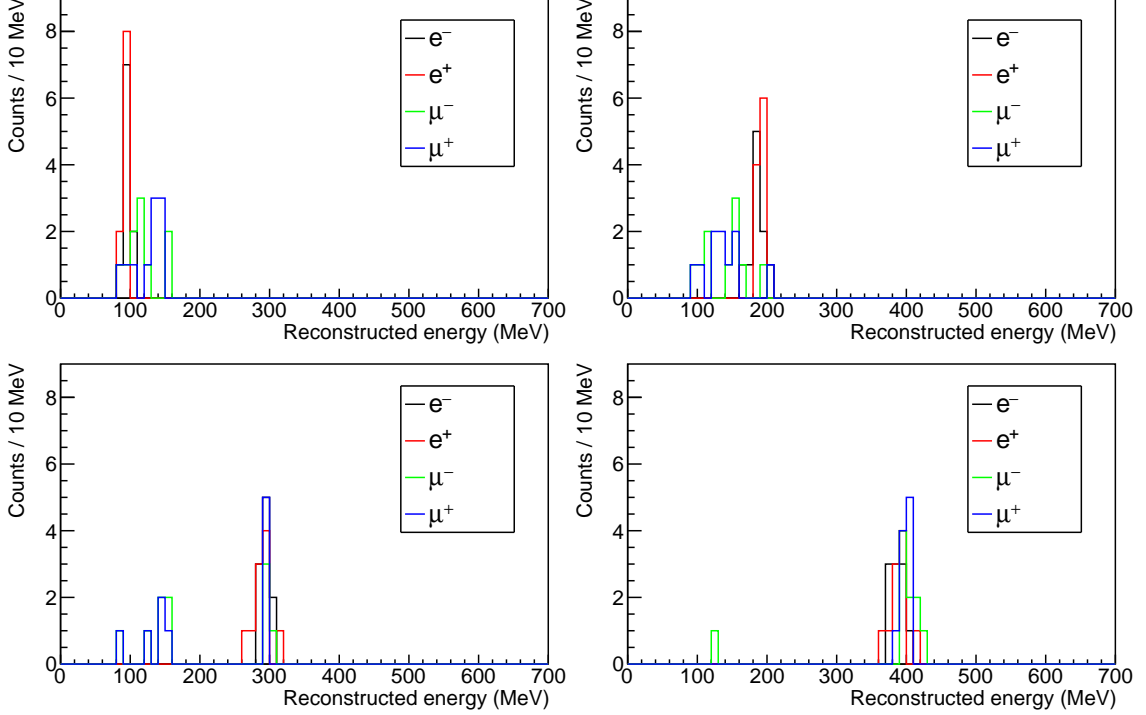


Figure 9: Reconstructed energy spectra from fitQun on simulated Cherenkov events in the HyperK geometry. Shown are the results for different charged leptons with different input energies (in MeV): 100 (top left), 200 (top right), 300 (bottom left), and 400 (bottom right).

energies. There is only one outlier left for 400-MeV muons, out of 20 events. The general behaviour for the reconstructed muon energies can be due to that a muon requires a higher kinetic energy to produce Cherenkov radiation, due to its larger mass compared to an electron. For the two leptons, the minimum threshold energies are as follows:

$$E_{\mu} \geq 54.9 \text{ MeV, and} \quad (13)$$

$$E_e \geq 0.266 \text{ MeV.} \quad (14)$$

3.4 Adaptation to the ESSnuSB near detector geometry

One of the goals of this project is to investigate the efficiency of the near detector to properly identify the particles during the reconstruction process as discussed above. Another goal is to construct the migration matrices of the input energy versus the reconstructed energy of the leptons, and to compare them, e.g for different detector sizes.

The first step was to change the geometry of the near detector. The four different geometries analysed in this project are given in Table 2, with the dimensions similar to the ones examined in Ref. [6]. Electrons and negatively-charged muons with 10 different energies from 100 MeV to 1000 MeV were simulated, with initial positions sampled out of a homogeneous distribution inside the tank and a uniform direction vector from one flat wall of the cylindrical tank to the other. 1000 events for each

Table 2: The four different sets of geometrical parameters for the near detector study in this work.

Geometry type	A	B	C	D
Tank radius (m)	3.75	6.25	3.75	6.25
PMT coverage (%)	40	40	40	40
PMT diameter (inches)	4	4	8	8
Tank height (m)	10	10	10	10
Number of PMTs	15614	30780	3956	7378

Table 3: Detector and particle gun settings for Cherenkov event simulation in WCSim.

Parameters	Value
Detector geometry	A, B, C, D
Flavour	e^-/μ^-
Lepton energy	100 to 1000 MeV, in 100-MeV increments
Starting position	homogeneous distribution
Momentum direction	$(x, y, z) = (0, 0, 1)$, downstream
Events per energy setting	1000

geometry setting were simulated. These simulation parameters are summarized in Table 3. The default tuning parameters of fitQun, adapted for the HyperK geometry, were used as a starting point for this project. The possibility to do multi-ring fits was deactivated and only single-ring fits were performed. A computing cluster at Lund University with multiple nodes was used for both simulation and reconstruction, where each node hosted 16 cores of AMD Opteron(TM) Processor 6220 with a speed of 2999.780 MHz and 2048 KB cache size. The RAM on each node was 32 GB. Due to compatibility issues, multithreading was not enabled and thus a single core were used for each set listed in Table 4.

For each energy and detector geometry setting, WCSim required 30-40 minutes of computation time for 1000 events. The computation times for fitQun reconstruction for each lepton flavour and geometrical setting are listed in Table 4. The reconstruction time scaled with the input lepton energy. Also, for the same energies, the reconstruction time was longer for the 4-inch PMTs and the large tank size. In addition, the muon events had a longer reconstruction time compared to the electron events for the same detector geometry and energy.

4 Results and Discussion

4.1 Lepton identification performance

The ability of fitQun to correctly identify the flavour of the charged leptons was examined via likelihood ratios as a function of the total charge Q_{tot} deposited in the PMTs, as shown in Fig. 10. The energy and the geometrical dependence (i.e. the initial position of the lepton) on the particle identification accuracy are reflected in Q_{tot} . As expected, it is more difficult to obtain a correct particle identification

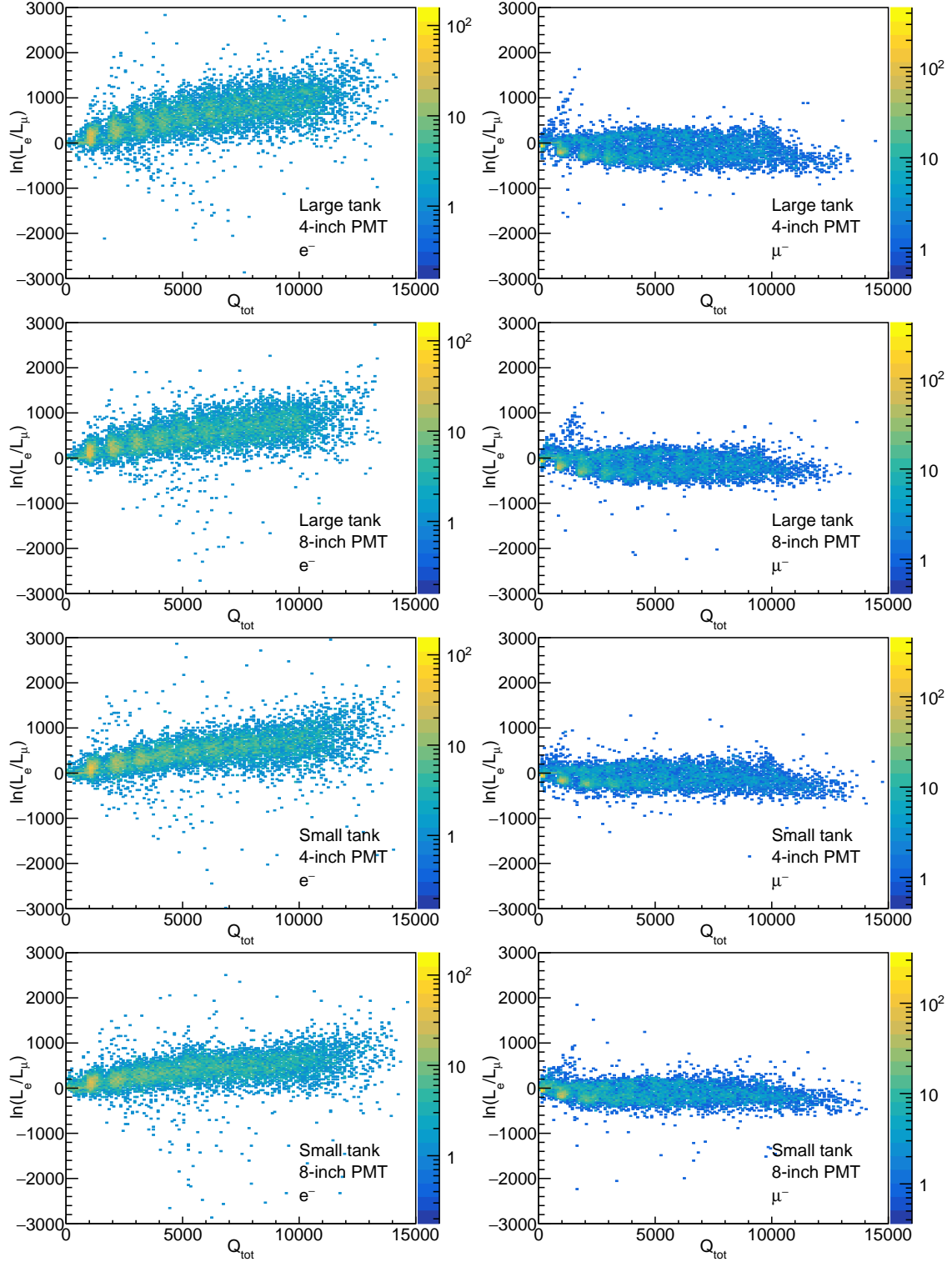


Figure 10: Lepton flavour likelihood ratios from fitQun for electrons (left column) and muons (right column) for the different geometry settings and as a function of the total charges deposited in the PMTs. Each cluster of counts in the distributions corresponds to the input energy of the leptons as described in Table 3.

Table 4: Computation hours for the fitQun reconstruction on 1000 events with different geometrical and lepton flavour settings.

Tank size	PMT radius	Flavour	Reconstruction time range (hours)
small	4-inch	e^-	13.7 - 21.1
small	8-inch	e^-	3.8 - 5.3
large	4-inch	e^-	26.1 - 39.2
large	8-inch	e^-	6.7 - 9.6
small	4-inch	μ^-	15.2 - 26.9
small	8-inch	μ^-	3.9 - 6.4
large	4-inch	μ^-	30.0 - 52.2
large	8-inch	μ^-	7.4 - 12.2

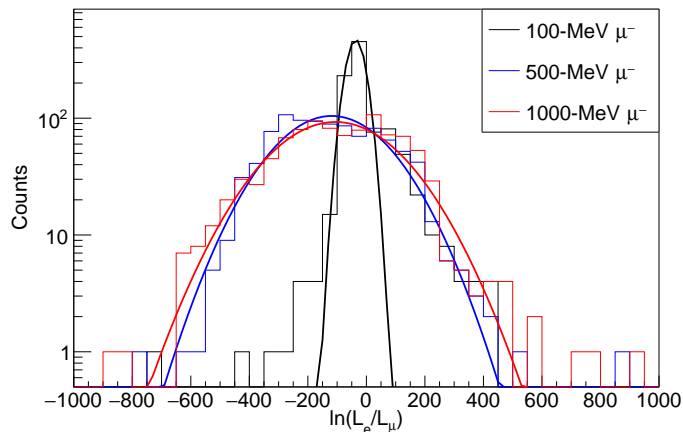


Figure 11: Likelihood ratios of electron/muon hypotheses from fitQun for simulated muons at 3 different energies. The distributions were fitted with Gaussian functions.

(PID) at low Q_{tot} . For the electron, there is a strong correlation between the PID likelihood difference and Q_{tot} for all different geometry settings. Since Q_{tot} depends on the input energies, it can be assumed that the accuracy the electron PID increases with input energy. For muons, the correlation between the PID likelihood difference and Q_{tot} is smaller than for electrons. On the other hand, there are other energy- and geometry-dependent factors which induce flavour misidentifications for both the electrons and the muons.

The distributions of PID likelihood ratios, as a function of the lepton input energy were also analysed. A few examples are shown in Fig. 11. The events where $\ln(L_e/L_\mu) < 0$ are correctly identified as muons, and all others may be interpreted as misidentified electron events. The opposite applies for the PID likelihood distributions with electrons. It is shown that the likelihood distributions become wider with high input energies. The distribution widths are similar for 500 MeV and 1000 MeV but it is much narrower for 100 MeV. In order to measure actual misidentification ratio numerically, further analysis is done below.

The large misidentification ratios for muons at low energies shown in Fig. 10 and Fig. 11 might be explained by the higher kinetic energy threshold for muons to produce Cherenkov radiation than electrons, as stated in Eq. 13.

The misidentification percentages for both muons and electrons for each geometric

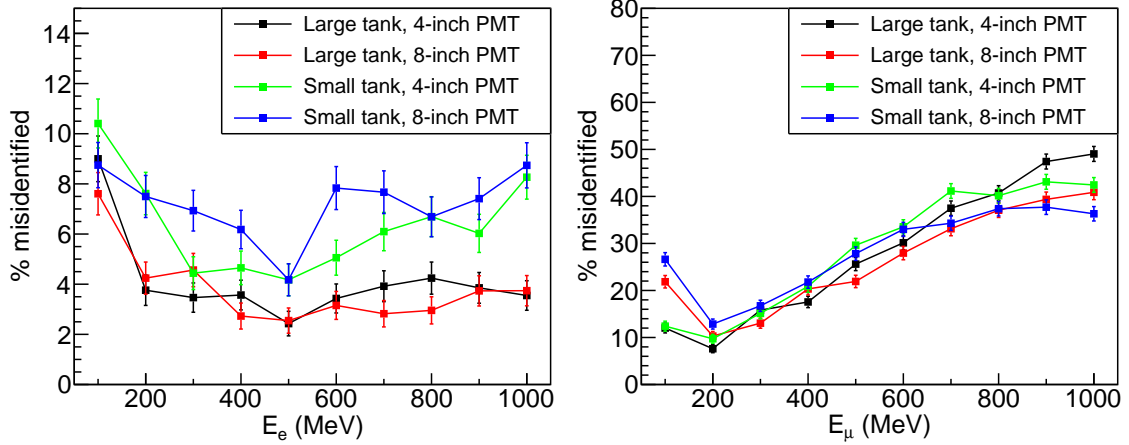


Figure 12: Lepton misidentification percentages as a function of energy from fitQun for electrons (left) and muons (right) for different detector geometries.

setting can be measured as well (see Fig. 12). It is clear that electron events have a lower misidentification ratio than the muon events in general, from 4% to 10%. The muon events, on the other hand, have a misidentification ratio from 10% to 50%. The results show that the misidentification ratio is stable for electrons, more or less independent on their energies. One can observe that the misidentification ratio is smaller for the large tank compared to the smaller tank, and independent of the PMT size. This is an interesting result for the design of the detector concerning the PMT choices. It is also shown that misidentification percentages are not dependent on geometry settings for muon. On the other hand, little difference in misidentification ratios was found for muons among different geometries. It is intriguing that for muons, the misidentification ratio increases as a function of energy starting from 200 MeV. This gives a possible indication that the projections of Cherenkov rings from muons were not developed properly at the detector walls at the higher energies.

4.2 Geometrical effects on the reconstruction performance

The likelihood ratios and the reconstructed Z position for both electrons and muons at 200 MeV and 700 MeV were also extracted (see Fig. 13). As before, the events above the horizontal dashed line represents particles that were identified as electrons and those below represent muon events. It can be seen in these histograms that the likelihood ratio distribution does shift away from the dashed line for high electron energies. This can be due to more photons being created at higher energies. This interpretation is also consistent with the results shown in Fig. 10. However, the misidentification ratio increases as the reconstructed Z position gets closer to the downstream wall. This phenomenon is analogous to the aforementioned effect of the Cherenkov rings not being developed properly for the identification to work well. Similar trends can be observed for muons, except that the Z position from which the misidentification ratio increases occurs at a lower value for high-energy muons. This result offers a reasonable explanation for the increasing trend of the misidentification percentage for muons as shown in Fig. 12.

The next step to improve the misidentification ratio would be to perform a 2D cut in

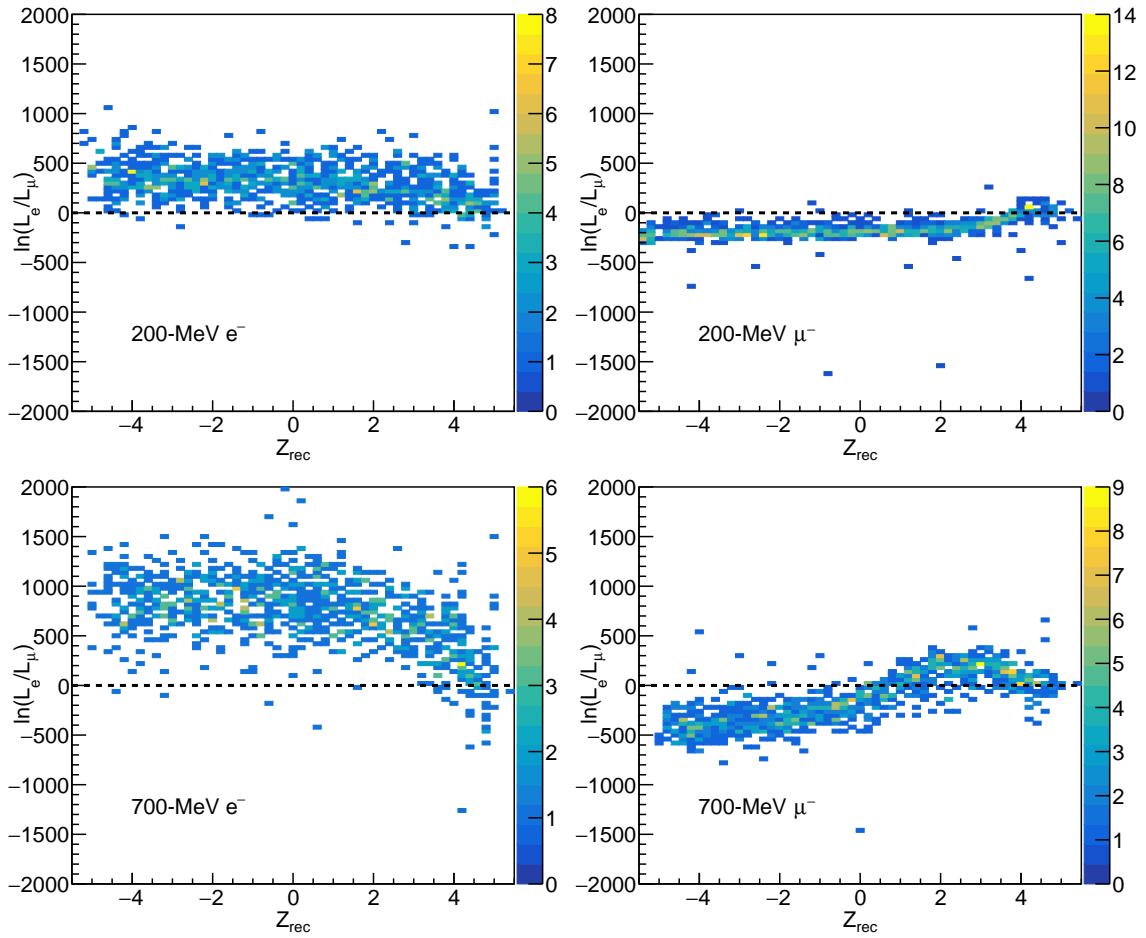


Figure 13: Electron-to-muon likelihood ratios from fitQun for electrons (left column) and muons (right column) at low and high energies as a function of the reconstructed z-positions. The events were simulated in a large water tank with 4-inch diameter PMTs.

the $\ln(L_e/L_\mu)$ vs Z plane. However, even if the misidentification ratio can be reduced in this way, it could also influence the efficiency which in turn could increase the systematic uncertainty. This effect will be studied further in the future.

The misidentification ratios can potentially also be reduced by considering more information in the fitQun output. In this project, only the reconstructed Z -position, and the total charge, Q_{tot} were considered together with the likelihood ratio. However, other factors such as the particle creation time, the radial vertex position and the momentum direction could also be used to find efficient PID cuts.

Reducing the background is also important. One of the most crucial backgrounds that cause misidentification in a Cherenkov detector is the decay of a muon into an electron together with the creation of muon and electron neutrinos. These events produce electrons with high kinetic energy that produce Cherenkov radiation which can give rise to misidentification of muons as electrons.

4.3 Preliminary migration matrices

The migration matrices for both electrons and muons for each detector geometry were constructed (see Fig. 14). It is clear that the relation between the reconstructed energy and the input energy is dominantly linear, but that the reconstructed energies are approximately half of the input energies. The likely reason is that the HyperK geometry tune was used instead of making a dedicated new ESSnuSB near detector tune as part of this project. Several steps should be done to make a new tune, these include investigations of the charge, angular, and time responses of the PMTs.

Comparing the migration matrices for each geometry setting shows that the muon matrices do not show any significant geometry dependence. However, the electron matrices are more dependent on the geometry and show a tendency for incomplete energy reconstruction for the smaller tank size.

5 Conclusion

The neutrino oscillation experiment ESSnuSB aims to measure the CP violation phase in the lepton sector with an intense neutrino beam from ESS in order to provide a possible explanation for the matter antimatter asymmetry in the Universe. In order to do this, a near detector is needed to measure the flux of the neutrinos and to decrease the systematic uncertainties of the oscillation measurement at the far detector.

For this purpose, a design study of the near detector in the form of a water Cherenkov detector was carried out. In this project, the tank size, and the PMT size, was investigated in the energy range from 100 MeV to 1000 MeV. Each geometry was simulated using the WCSim simulation software based on the Geant4 framework. The reconstruction of the events was done using fitQun software.

The misidentification percentage for different geometries as a function of energy was extracted. The misidentification percentage is relatively stable for electrons while it

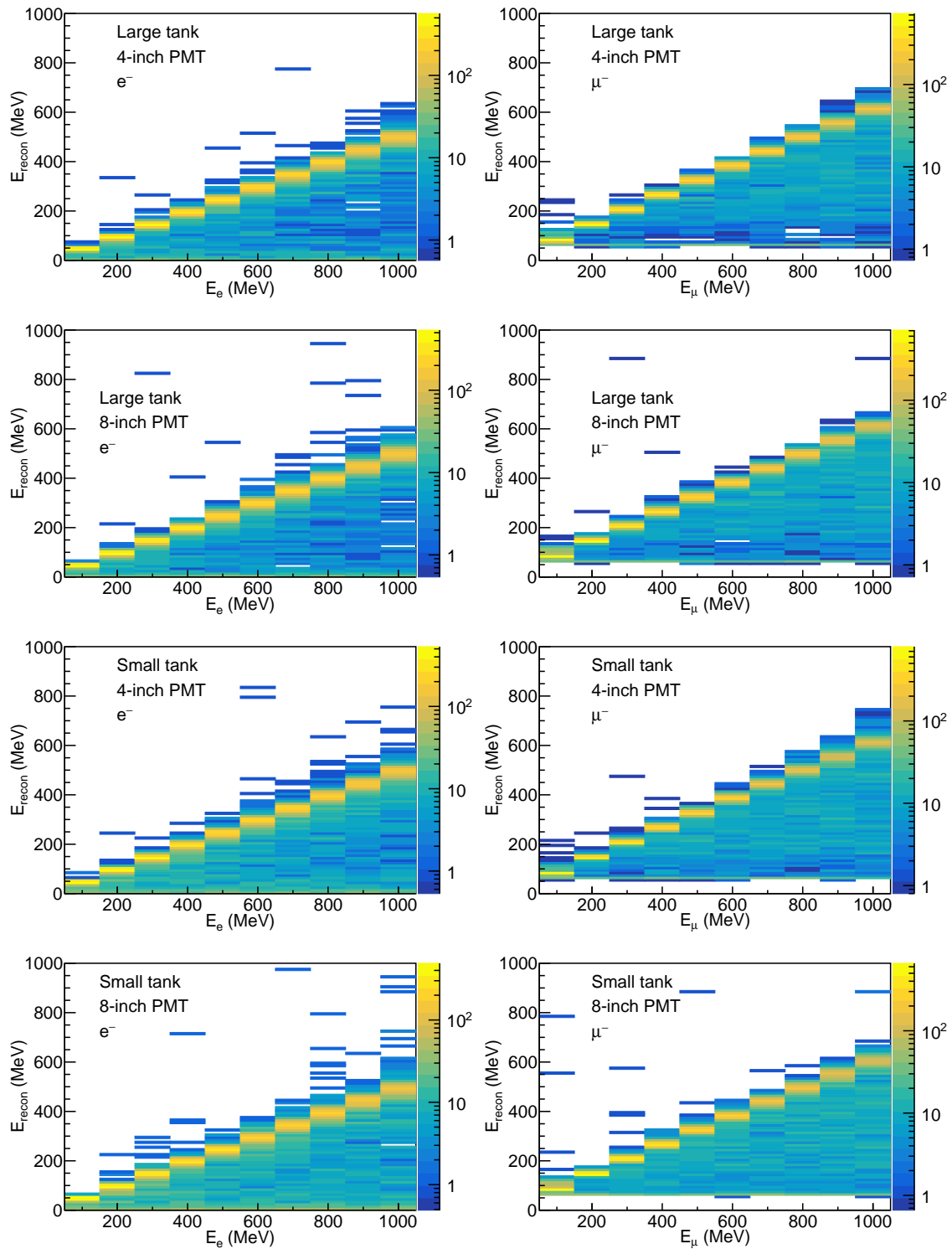


Figure 14: Migration matrices of reconstructed charged lepton energies as a function of the input energies for both electrons (left column) and muons (right column) and for the different detector geometries.

increases with increasing energy for muons. For electrons, the misidentification ratio is nearly independent on the PMT size and is more dependent on tank size. Future design work should thus focus more on tank size rather than the PMT size. It was also concluded that 2D cuts involving the fitQun output variables could improve the misidentification ratio.

Finally, migration matrices were constructed for each geometry. The reconstructed and input energy shows a proportional behaviour, but the reconstructed energy is approximately half of the input energy. To improve on this situation, a dedicated tune is planned for ESSnuSB.

References

- [1] <https://home.cern/science/physics/higgs-boson>.
- [2] <https://www.nobelprize.org/prizes/physics/2015/press-release/>.
- [3] J. M. Cline, arXiv:hep-ph/0609145.
- [4] A.D. Sakharov, “Violation of CP invariance, C asymmetry, and baryon asymmetry of the universe”, Sov. Phys. Usp. 34, 392 (1991).
- [5] L. Jonsson, “Lectures in Particle physics”, Lund University (2010).
- [6] A. Burgman, “A simulation study on the design of the Cherenkov near detector of the proposed ESS ν SB”, Master’s thesis, Lund University (2015).
- [7] M. Tanabashi et al., Phys. Rev. D 98, 030001 (2018).
- [8] <http://www.hyper-k.org/en/physics/phys-hierarchy.html>.
- [9] Y. Fukuda et al. (Super-Kamiokande Collaboration), Phys. Rev. Lett. 81, 1562 (1998).
- [10] <https://www.taborelec.com/pion-decay-solution-note>.
- [11] P. Coloma and E. Fernandez-Martinez, “Optimization of neutrino oscillation facilities for larger θ_{13} ”, J. High Energ. Phys. 2012, 89 (2012).
- [12] K. Chakraborty, K.N. Deepthi, and S. Goswami, “Spotlighting the sensitivities of the Hyper-Kamiokande, Dune and ESS ν SB”, Nuclear Physics B 937, 303 (2018).
- [13] E. Wildner, ESSnuSB Collaboration, Nuclear and Particle Physics Proceedings 265–266, 195 (2015).
- [14] M. Dracos, ESSnuSB project, Nuclear and Particle Physics Proceedings 273–275, 1726 (2016).
- [15] E. Baussan et al., arXiv:1309.7022.
- [16] J.D. Jackson, *Classical Electrodynamics*, 3rd edition, (John Wiley and Sons, New York (1998)).

- [17] J. Kameda, “Neutrino interaction measurement in 1kton water Cherenkov Detector in K2K Experiment”, Proceedings of the RCCN International Workshop (2004).
- [18] T. Dealtry, A. Himmel, J. Hoppenau, and J. Lozier, “Simulating water Cherenkov Detectors using WCSim” (2016).
- [19] L. Agostino et al., “Future large scale water-Cherenkov detector”, Phys. Rev. ST Accel. Beams 16, 061001 (2013).
- [20] S. Tobayama, “An Analysis of the Oscillation of Atmospheric Neutrinos”, PhD thesis, University of British Columbia (2016).
- [21] A. D. Missert, “Improving the T2K Oscillation Analysis With fitQun: A New Maximum-Likelihood Event Reconstruction for Super-Kamiokande”, IOP Conf. Series: Journal of Physics: Conf. Series 888, 012066 (2017).